



A novel efficient visible-light-driven double Z-scheme PANI/Ag₃PO₄/CNO heterojunction photocatalyst mediated by PANI and in situ grown AgNPs

Mingyuan Xie¹ and Tailiang Zhang^{1,*}

¹ College of Chemistry and Chemical Engineering, Southwest Petroleum University, Chengdu 610500, Sichuan, People's Republic of China

Received: 2 September 2019

Accepted: 23 November 2019

Published online:

7 December 2019

© Springer Science+Business Media, LLC, part of Springer Nature 2019

ABSTRACT

Degrading organic pollutants from semiconductor photocatalysis technology is an attractive alternative to other advanced oxidation technologies, thanks to its green energy characteristics, mild reaction conditions, freedom from secondary pollution and ability to produce rich free radical species. Herein, we demonstrate the efficient degradation of several organic dyes and their mixture, which is achieved over a double Z-scheme PANI/Ag₃PO₄/g-C₃N₄-O (CNO) heterojunction catalyst and driven by visible light. With this degradation, the apparent degradation rate for RhB was up to 0.2668 min⁻¹, which was approximately 1.31, 2.68, 5.28 and 17.12 times faster than those of PANI/Ag₃PO₄, Ag₃PO₄/CNO, Ag₃PO₄ and CNO, respectively. It also exhibited excellent activity for mixed dyes. Furthermore, the double Z-scheme heterojunction photocatalytic system built around Ag₃PO₄, which was presented and confirmed by researching the band structures of the three semiconductors and conducting radical scavenging experiments, greatly accelerates the transfer of photogenerated electrons on the conduction band of Ag₃PO₄; therein, both PANI and in situ grown AgNPs act as electron mediators, thereby improving the activity and stability of Ag₃PO₄. This work puts forward a novel perspective for heightening the activity and stability of perishable photocatalysts for organic dye effluent and other organic pollutant treatments.

Address correspondence to E-mail: TailiangZhang@outlook.com

Introduction

Modern society faces severe energy and environmental problems. On the one hand, fossil energy seriously pollutes the environment during exploitation and utilization. On the other hand, enormous fossil energy is consumed in the process of using traditional technology to treat environmental pollution. Solar-powered semiconductor photocatalytic technology is considered to be the most promising method for mitigating the two aforementioned problems because it can directly convert solar energy into chemical energy to degrade environmental pollutants and produce “green” energies, does not generate secondary pollution and is highly efficient [1, 2]. However, the short lifetime of photogenerated charges and the poor solar light harvesting efficiency hinder the practical application of this technology due to the aforementioned problems [3–5]. In this context, Ag_3PO_4 (AP), which exhibits a striking quantum efficiency of 90% at 420 nm and can absorb light with a wavelength shorter than 530 nm, is a compelling candidate for visible-light-driven organic contaminant decomposition and oxygen production from water [6–8]. Nevertheless, its susceptibility to photocorrosion, limited conduction band (CB) position and high synthetic costs make its large-scale application difficult [6, 9]. To minimize these drawbacks, some researchers have exploited precious-metal cocatalytic systems [10] and carbon nanomaterial heterojunction photocatalytic systems [11–13]; however, neither of these strategies substantially reduces the excessively high cost of preparing the catalyst. Moreover, although relatively low-cost traditional semiconductor heterojunction photocatalytic systems, such as AP/Cr-SrTiO₃ [14], AP/CeO₂ [15] and AP/LaFeO₃ [16], can improve the activity of the system by accelerating the transfer of photogenerated charges on the AP surface, these systems do not contribute to the photostability of AP and the reducibility of photogenerated electrons on the CB of AP. Furthermore, the formation of such heterojunctions weakens the oxidizability of photogenerated holes on the valence band (VB) of AP.

Fortunately, unlike the traditional heterojunction photocatalytic systems, in Z-scheme heterojunction photocatalytic systems, which include AP/WO₃ [17], AP/MoS₂ [18] and AP/CuBi₂O₄ [19], the photogenerated electrons on AP, which have weak

reducibility, can undergo recombination with the photogenerated holes on another semiconductor (e.g., SnSe₂ or MoS₂), which have weak oxidizability, leaving stronger photogenerated holes and electrons [20, 21]. This system put forwards an efficient method to overcome the shortcomings of the conventional heterojunction photocatalytic systems. As a low-cost graphene-like layered nanomaterial with high stability, no metal and visible light driven, g-C₃N₄ (CN) with a moderate band gap of approximately 2.31–2.86 eV is widely used in the photocatalytic degradation of organic pollutants and the decomposition of water to prepare hydrogen [22–24]. In particular, compared with AP, CN has a more negative CB potential of approximately – 0.79 V to – 1.44 V, which is related to its specific structure [25, 26]; that is, it can easily utilize free oxygen adsorbed onto the surface of the catalyst to produce more active species to enhance the photocatalytic activity of the system [27, 28]. Du et al. synthesized a direct Z-scheme AP-based hybrid material modified with CN nanocrystals (CN-NCs). Compared with pure AP and CN-NCs, the AP/CN-NCs exhibit greater activity [29]. Similarly, CN can also form a direct Z-scheme heterojunction with other semiconductors to enhance their photocatalytic activity [30–32].

However, the phenomenon of slow charge transfer at the interface of two semiconductors of a Z-scheme heterojunction system formed by direct contact is commonly observed; this slow charge transfer greatly reduces the photocatalytic activity of this system [33]. To minimize this disadvantage, an electron mediator, such as a noble metal [34–37] or carbon nanomaterial [38–40], can be introduced into this system to accelerate the charge transfer. Polyaniline (PANI) doped with a protonic acid is a semiconductor polymer with high conductivity, good stability and low cost [41, 42], making it one of the most satisfactory electron mediators for accelerating charge transfer in a binary direct Z-scheme photocatalytic system. However, to the best of our knowledge, the literature contains no similar reports. In addition to acting as an electron mediator, PANI can also function as a catalyst in semiconductor heterojunction photocatalytic systems [43–45]. Notably, Hu et al., for the first time, used the chemisorption method to hybridize Ag₂CO₃ and PANI to obtain a Z-scheme heterojunction photocatalyst; compared with pure Ag₂CO₃, the Ag₂CO₃/PANI clearly exhibited enhanced photocatalytic activity in the

degradation of methyl orange (MO) under visible-light illumination [46].

Here, we successfully prepared a double Z-scheme heterojunction photocatalytic system constituted of AP, PANI and g-C₃N₄-O (CNO) via a temperate in situ precipitation method and assessed its catalytic activity through decomposing Rhodamine B (RhB), methylene blue (MB), MO and their mixture under visible-light exposure. In particular, PANI plays two roles in this system: It forms a Z-scheme heterojunction with AP, and it functions as an electronic mediator between the Z-scheme heterojunction formed by AP and CNO. Comparing the photostabilities and photocatalytic activities of the AP, AP/CNO and PANI/AP systems, those of the PANI/AP/CNO system were heightened. The amelioration was due to the efficient transfer of electrons on the AP surface and the improvement of photo-generated electron reducibility by a double Z-scheme heterojunction photocatalytic mechanism, which we presented and confirmed via researching the band structures of the three semiconductors and conducting radical scavenging experiments.

Experimental

Reagents

A 5% Nafion solution was purchased from the Alfa Aesar Chemical Co., Ltd. Sulfosalicylic acid-doped PANI was purchased from the Wuhan Yuancheng Gongchuang Technology Co., Ltd. Other reagents were purchased from the Chengdu Chron Chemical Co., Ltd. All of the reagents were used as received without further purification.

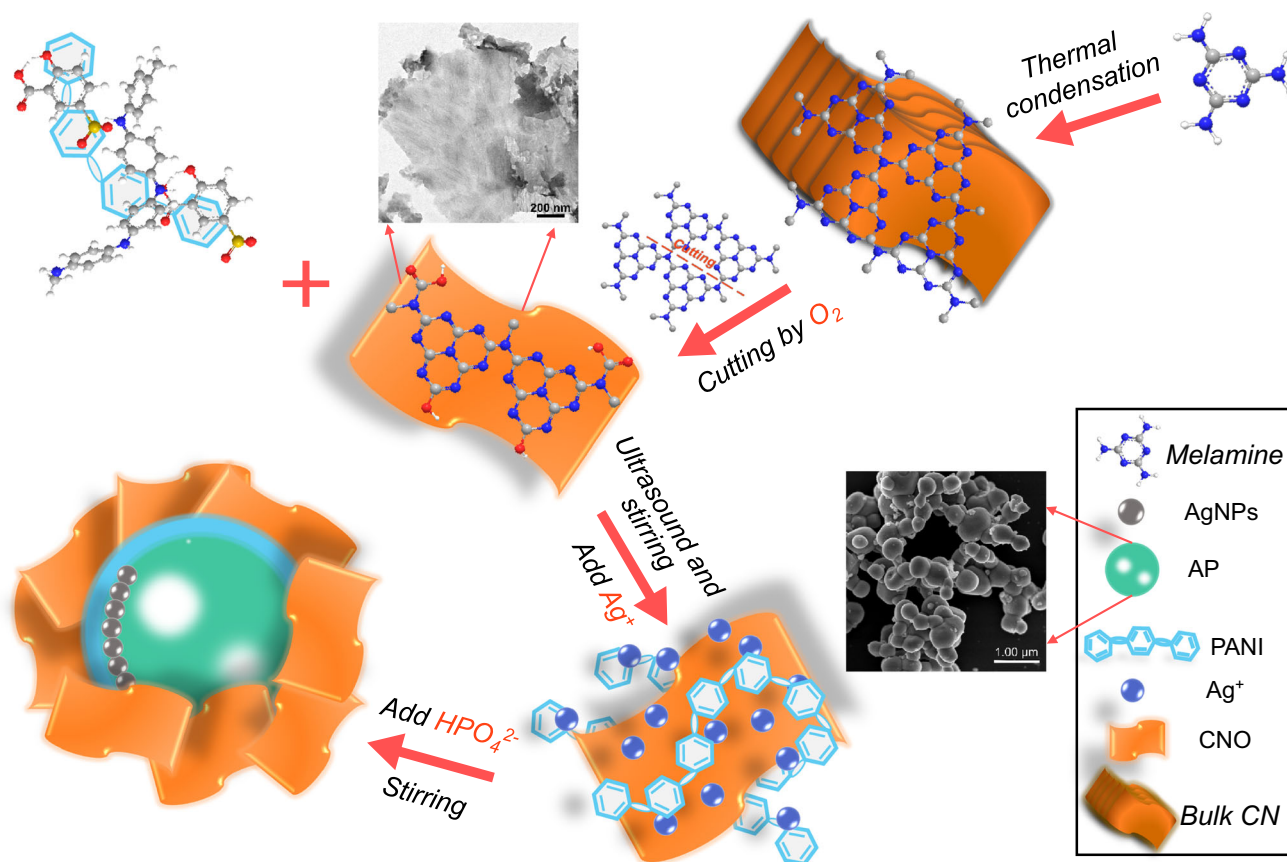
Synthesis of PANI/AP/CNO

As shown in Scheme 1, first, bulk CN (b-CN) was prepared via the thermal condensation of melamine (550 °C, 240 min, 2 °C/min) [47]. Second, multilayer CNO was synthesized by the oxidative cutting of the prepared b-CN (550 °C, 140 min, 5 °C/min). The success of this cutting process was indicated by a gradient change of the sample colour from yellow to light yellow. Additionally, AP was prepared according to a literature procedure with minor modifications [6], and the PANI/AP/CNO was prepared by a similar in situ precipitation method. As shown in

Fig. S1, by changing the contents of CNO and PANI in the composites, we found that PANI/AP/CNO has the highest photocatalytic activity when the mass ratio of PANI, AP and CNO is 5:100:30. The following is the preparation method of PANI/AP/CNO in this ratio: AgNO₃ (1.5 mmol), PANI (10.5 mg) and CNO (62.8 mg) were dissolved in 30 mL of water in a 100-mL three-necked flask, and the resultant mixture was ultrasonicated in conjunction with mechanical agitation for 30 min at room temperature. The ultrasonicator was then turned off, and vigorous stirring was continued for 2 h. Both the rich oxygen-containing functional groups on the surface of CNO (Fig. 1q, Fig. S2) [48] and the lone pairs of electrons on the outer N atoms of PANI can electrostatically attract Ag⁺ ions [45, 49]. The Ag⁺ ions adsorbed onto the CNO and PANI were subsequently precipitated and underwent in situ growth by the dropwise addition of 10 mL of Na₂HPO₄ (0.1 M) aqueous solution, followed by stirring for 1 h to form PANI/AP/CNO ternary composites in which AP was encapsulated by CNO and PANI. The PANI, AP and CNO actual contents were determined to be 7.99 wt%, 71.27 wt% and 20.74 wt% by inductively coupled plasma optical emission spectrometry (ICP-OES), respectively. In addition, PANI/AP and AP/CNO composites were prepared using the same method but without CNO and PANI, respectively.

Characterizations

Powder X-ray diffraction (XRD) patterns of the as-prepared samples were determined with a PANalytical X'Pert Pro MPD diffractometer equipped with a Cu-K α radiation source operated at 40 kV and 20 mA. Raman spectroscopy of PANI/AP/CNO was performed with a Renishaw inVia laser confocal Raman spectrometer. Fourier transform infrared (FT-IR) spectra were recorded on a WQF-520 spectrometer in the wave number range from 400 to 4000 cm⁻¹ with a resolution of 2 cm⁻¹ and using KBr as the beam splitter. The morphologies of the as-prepared samples were observed by field-emission scanning electron microscopy (FE-SEM, SU8010) and transmission electron microscopy (TEM, Tecnai G2 F20 S-TWIN). X-ray photoelectron spectroscopy (XPS) was conducted on an ESCALAB 250XI (Thermo Fisher) with an Al-K α source (the measurement error was within ± 0.2 eV), and energy-dispersive spectroscopy (EDS, SU8010) was utilized to characterize



Scheme 1 Schematic of the synthetic process to form PANI/AP/CNO.

the chemical constituents and elemental valence states of the PANI/AP/CNO. Analysis of the true content of each component in the PANI/AP/CNO was conducted with an Agilent ICPOES730 ICP-OES. UV-Vis diffuse reflectance spectroscopy (UV-Vis DRS) of the as-prepared samples was conducted with a Lambda850 UV-Vis spectrophotometer using BaSO₄ as the baseline. The photoluminescence (PL) spectra (FluoroLog-3, Jobin-Yvon) were used to assess the lifetimes of the photoinduced charge carriers of the as-prepared samples. Electron paramagnetic resonance (EPR) spectra were obtained on a Bruker A300-10/12 electron paramagnetic resonance spectrometer. Photoelectrochemistry measurements were carried out using a CS350 electrochemical workstation (Corrtest Instruments Corp., Ltd., Wuhan) with a standard three-electrode system. The preparation of the working electrode is described in the Supporting Information, along with the methods used to construct the transient photocurrent response spectrum, the Mott-Schottky curve and the Nyquist

diagram from the electrochemical impedance spectroscopy (EIS).

Photocatalytic performance

Photocatalytic reactions were conducted at room temperature in a beaker (covered with aluminium foil), which was exposed to a 200 W LED mining lamp (≤ 16000 lm, HX-200 W) with a 420 nm cut-off filter. Typically, PANI/AP/CNO and an organic dye [RhB (20 mg/L), MB (20 mg/L), MO (10 mg/L) or their mixture (RhB:MB:MO = 6 mg/L:6 mg/L:3 mg/L)] solution were added to the beaker and stirred under a dark environment to accomplish an adsorption-desorption equilibrium. The reaction mixture was subsequently placed under light illumination (the distance between the white LED light and the reactor was 25 cm) and stirred. Three-millilitre aliquots were sampled and filtered through a 0.22 μm Nylon syringe filter and then analysed with a UV-Vis spectrophotometer (UV-1800, Shimadzu).

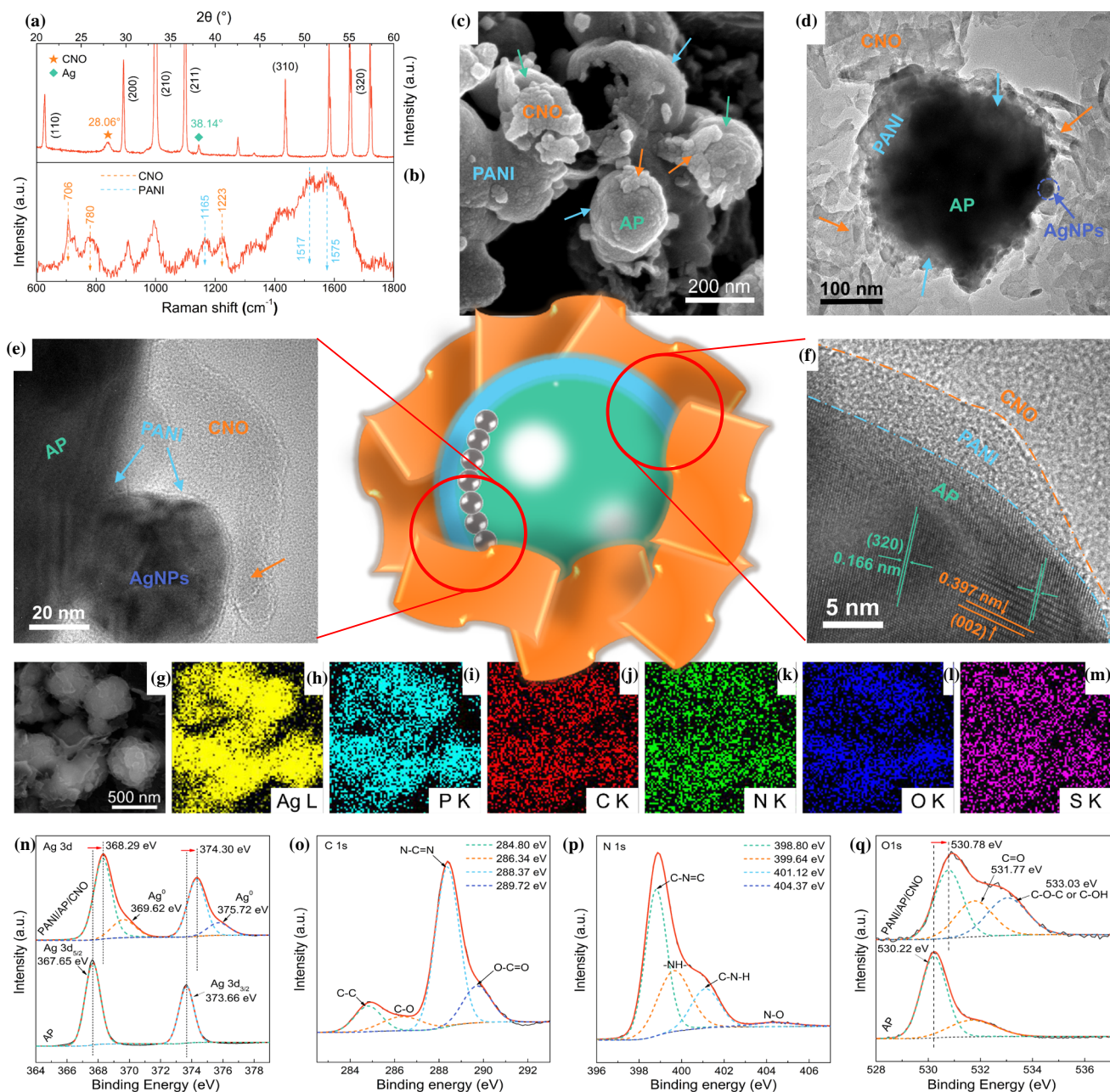


Figure 1 XRD pattern, Raman spectra and representative FE-SEM, TEM and HRTEM images, EDS maps and XPS spectra of PANI/AP/CNO: **a** XRD pattern; **b** Raman spectrum; **c**, **g** FE-SEM

images; **d**, **e** TEM images; **f** HRTEM image; **h–m** EDS elemental maps of Ag, P, C, N, O and S; and XPS spectra: **n** Ag 3d, **o** C 1s, **p** N 1s and **q** O 1s.

Results and discussion

Characterization of PANI/AP/CNO

Figure 1a shows that all of the diffraction peaks of AP in the XRD pattern of PANI/AP/CNO are consistent with the standard pattern (JCPDS No. 06-0505) [50]. The (002) peak of CN at 27.55° is attributed to the interlayer stacking reflection [22], and the intensities

of the (002) peak of CNO became weaker (Fig. S3). In the pattern of PANI/AP/CNO, the (002) peak of CNO was observed, which means that CNO was present in the composite; meanwhile, the Raman and the FT-IR characteristic peaks located at 706, 780, and 1223 cm^{-1} [51] (Fig. 1b) as well as 1324 cm^{-1} [52] (Fig. S2), respectively, and the O 1s XPS spectrum [53] (Fig. 1q) can also confirm this result. Interestingly,

compared with the (002) peak of CN at 27.55° , those of CNO and PANI/AP/CNO shift to 27.80° and 28.06° , respectively, suggesting that the CN can be further planarized by loading AP onto its surface or by continued heating to oxidize its edges to produce a large number of oxygen-containing functional groups [54, 55]. As shown in Fig. 1b, the characteristic Raman peaks at 1165 cm^{-1} , 1517 cm^{-1} and 1575 cm^{-1} correspond to the C–H bending of the quinoid ring, the stretching of C=N in the quinoid ring and the stretching of C–C of the para-distributed benzenoid ring of PANI, respectively [41]. The presence of PANI was further confirmed by the S 2p spectra (Fig. S5c) and N 1s spectra, which show a peak at 399.64 eV that corresponds to –NH– in the PANI backbone [41] (Fig. 1p), as well as the EDS elemental map (Fig. 1m).

The FE-SEM image of the pristine AP in Fig. S4a shows that it consists of irregular, smooth-surfaced nanoparticles that are almost interconnected and are 200–800 nm in diameter; some of the nanoparticles are spherical. Compared with the pure AP, AP in the composite exhibited a smaller crystallite size and a rougher surface (Fig. 1c). TEM micrographs of PANI/AP/CNO (Fig. 1d) reveal that, on the one hand, PANI organic films are uniformly coated on the surface of the AP crystallites [44]; on the other hand, lamelliform CNO is closely attached to the surface of the AP wrapped by PANI, and the three together form a novel AP–PANI–CNO structure. In agreement with these observations, the lattice fringes of 0.166 nm and 0.397 nm in the HRTEM images of PANI/AP/CNO in Fig. 1f are attributed to the (320) and (002) interplanar distances of AP and CNO [22], respectively. Moreover, EDS elemental maps in the FE-SEM show that the PANI/AP/CNO consists of six elements; the silver, phosphorus and oxygen elements constituting the AP are mainly distributed in the spherical region of Fig. 1g, whereas the carbon, nitrogen and sulphur elements constituting CNO or PANI are uniformly dispersed throughout the area (Fig. 1h–m), which is consistent with TEM observations. Compared with the point-contact structure of conventional composites [14, 16, 19], this novel cross-linked structure creates a tight and large contact interface among AP, PANI and CNO. Notably, PANI, which is highly conductive, and CNO, which exhibits a huge specific surface area, not only accelerate the separation and migration of photogenerated electron–hole pairs on the AP surface but also provide

more active sites for the degradation reaction [42, 54]. Interestingly, some metallic silver nanoparticles (AgNPs) with a diameter of only approximately 50 nm are distributed at the interface between the AP particles and the PANI film (Fig. 1d, e). These AgNPs likely stem from the lone pair of electrons on the outer N atom of PANI easily adsorbing Ag^+ ions and restoring them to AgNPs [49]. Evidence of this process is provided by the metal Ag diffraction peaks (JCPDS No. 04-0783) at 38.14° in the XRD patterns of PANI/AP and PANI/AP/CNO [45] and by the distinct characteristic peaks of AgNPs at 369.62 eV and 375.72 eV in the Ag 3d XPS spectrum [56] (Fig. 1n). These AgNPs distributed at the AP and PANI interfaces accelerate the separation and transfer of photogenerated electron–hole pairs between AP and PANI and between AP and CNO.

In agreement with the EDS elemental mapping results, the XPS survey spectrum (Fig. S5a) also shows that the PANI/AP/CNO consists of six elements. In the C 1s XPS spectrum of PANI/AP/CNO (Fig. 1o), the peaks at the binding energies of 286.34 eV and 289.72 eV demonstrate the rich oxygen-containing functional groups on the CNO surface [53]. In particular, compared with the Ag 3d, P 2p and O 1s peaks in the spectrum of pure AP, those in the spectrum of PANI/AP/CNO are shifted to higher binding energies (Fig. 1n, Fig. S5b and Fig. 1q), indicating a strong interaction between Ag_3PO_4 , PANI and CNO [18], which is consistent with the XRD and HRTEM results.

Performance of PANI/AP/CNO

We used RhB as a target pollutant to investigate the photocatalytic activity of PANI/AP/CNO. As shown in Fig. 2a, RhB itself exhibits good light stability, and compared with other samples, the PANI/AP/CNO exhibits greater visible-light catalytic activity (99.34% under identical conditions). This degradation process conforms to the pseudo-first-order kinetic model [18], and the apparent rate constant of each sample was calculated according to the kinetic fitting curve (Fig. 2b). Among the investigated samples, PANI/AP/CNO has the largest kinetic constant of 0.2688 min^{-1} , which is 1.31, 2.68, 5.28 and 17.12 times greater than those of PANI/AP, AP/CNO, AP and CNO, respectively. As shown in Figs. 2c, d and 3, for the purposes of enlarging the application range of PANI/AP/CNO, we conducted contaminant

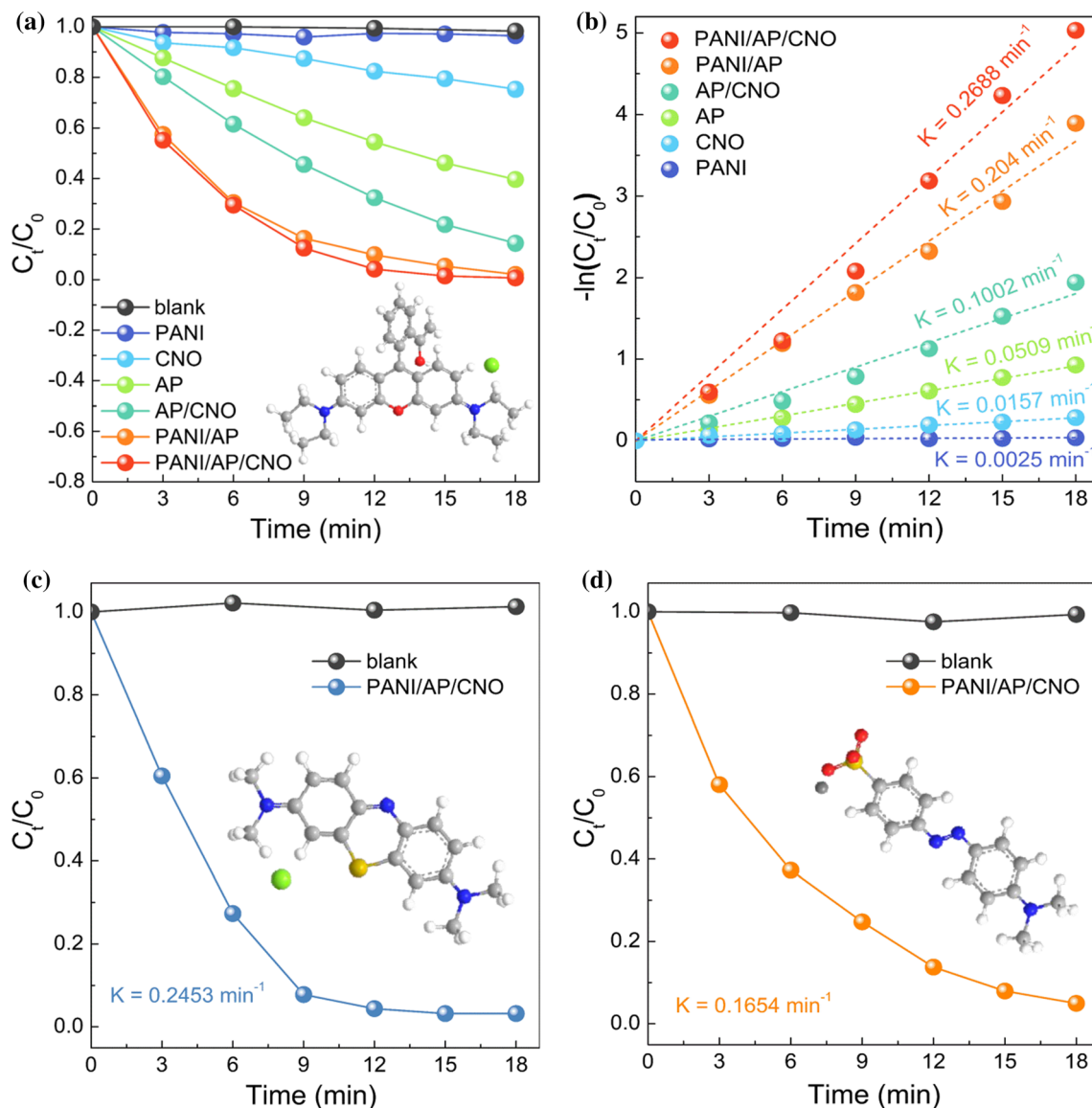


Figure 2 **a** Time profiles of visible-light-driven degradation, **b** pseudo-first-order kinetic model of visible-light-driven degradation kinetic fitting curves of RhB over PANI, CNO and AP as well as the AP/CNO, PANI/AP and PANI/AP/CNO

development experiments by degrading MB and MO as well as their mixture with RhB. The PANI/AP/CNO not only exhibited excellent photocatalytic activity towards MB, MO and RhB but also excellent activity for their mixture. Meanwhile, we further confirmed this result by measuring the total organic carbon (TOC) content during the degradation process of mixed dyes; specifically, the TOC removal efficiency was as high as 85.24% after 180 min, which indicates that PANI/AP/CNO also has strong photocatalytic degradation activity for colourless organic

composites; **c** time profiles of the visible-light-driven degradation of MB; **d** time profiles of the visible-light-driven degradation of MO.

pollutants. In addition, as shown in Table S1, we compared the degradation properties of PANI/AP/CNO with other Ag_3PO_4 -based photocatalysts under visible light for organic pollutants and listed their advantages and disadvantages.

The severe photocorrosion of pure AP remains one of the largest problems impeding its practical application. Therefore, we constructed this novel heterojunction system to not only improve the photocatalytic activity of AP but, more importantly, to enhance its photostability. To study the anti-

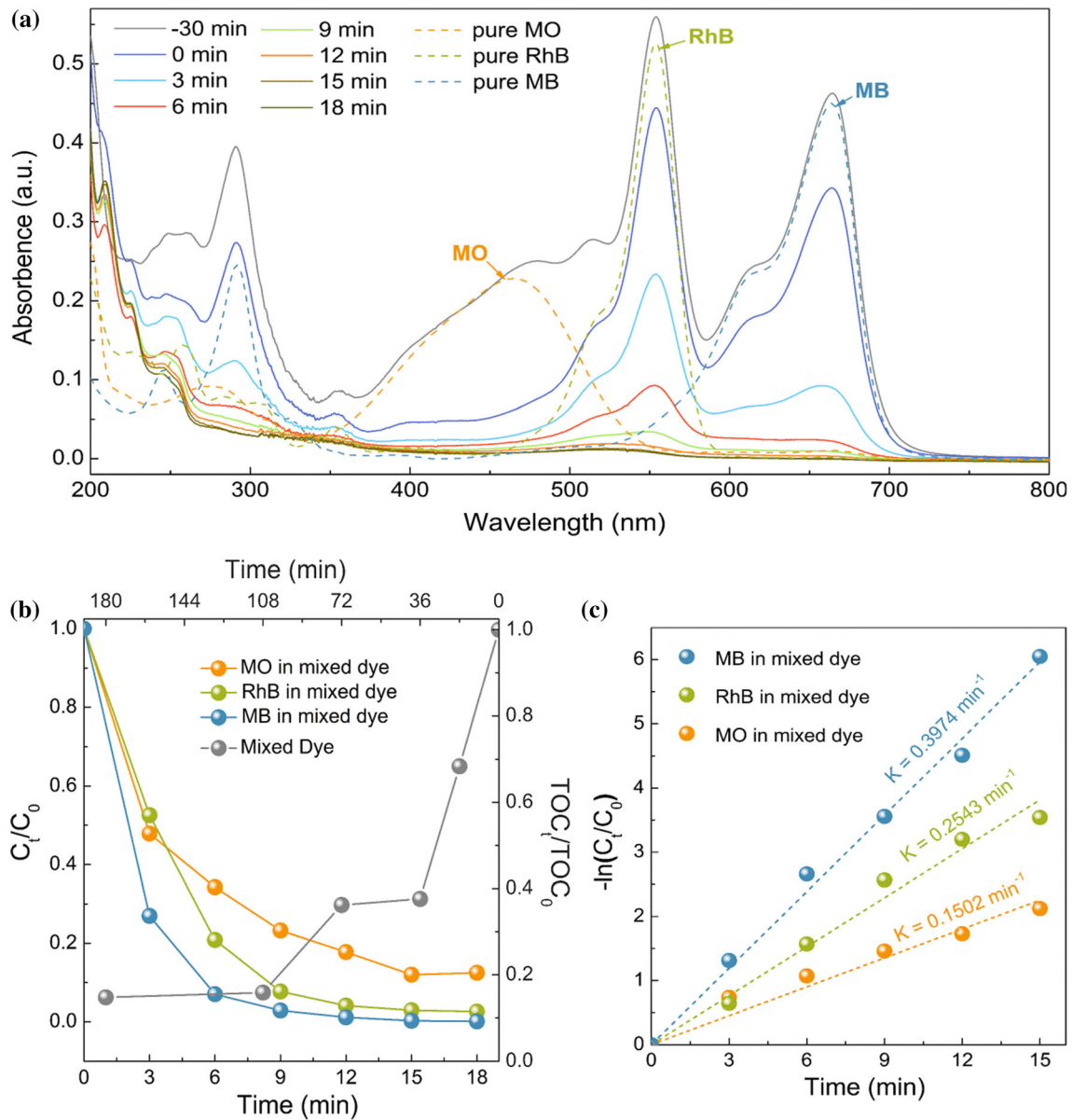


Figure 3 **a** UV–Vis spectroscopic spectra of pure RhB, pure MB and pure MO and the visible-light-driven degradation of their mixture over PANI/AP/CNO; **b** time profiles of the visible-light-driven degradation and TOC removal of mixed dyes over PANI/AP/CNO; and **c** pseudo-first-order kinetic model of visible-light-driven degradation kinetic curves of mixed dyes over PANI/AP/CNO.

photocorrosion of PANI/AP/CNO, we carried out cyclic degradation experiments using it and several comparative materials under the same degradation conditions (Fig. 4a). The PANI/AP/CNO exhibits superior activity to other photocatalysts after three degradation cycles (Fig. 4b). Nevertheless, as shown in Fig. 4c, after three uses, a stronger characteristic peak of metallic silver appears in the XRD pattern of PANI/AP/CNO compared with that in the pattern of AP. Combined with the results of the aforementioned

cyclic degradation experiments, these results indicate that, during the process of material preparation and photocatalytic degradation, the AgNPs in PANI/AP/CNO, due to the reducibility of PANI films wrapped on the surface of the Ag_3PO_4 , grow in situ at the interface between PANI and AP, whereas the metallic silver in AP is due to the free Ag^+ on the surface of AP being reduced by photogenerated electrons that have not been transferred in time [9]. The AgNPs in the former case can function as electron mediators,

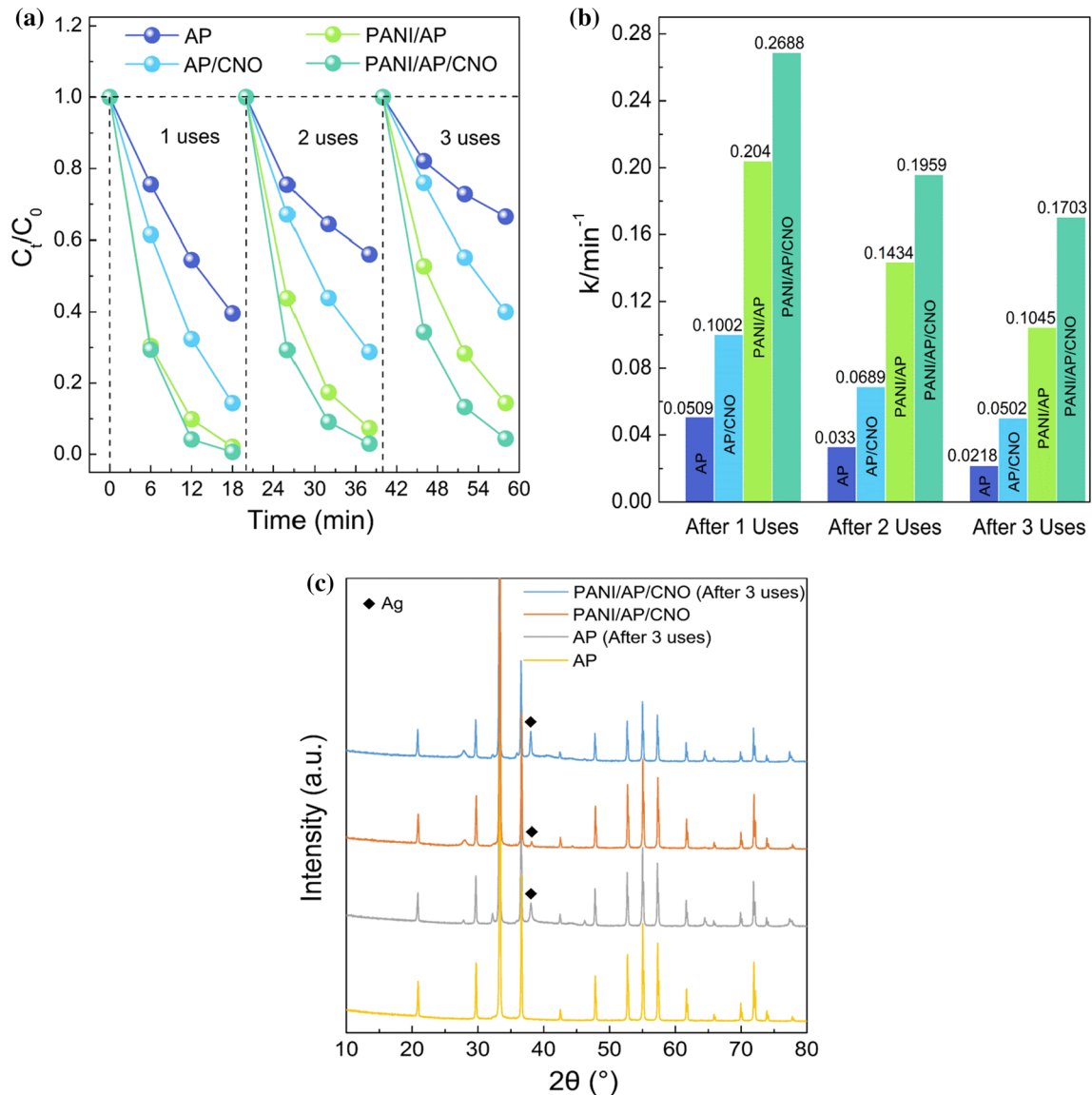


Figure 4 **a** Time profiles of cyclic visible-light-driven degradation of RhB over AP and the AP/CNO, PANI/AP and PANI/AP/CNO composites; **b** kinetic constants of the cyclic visible-light-driven degradation of RhB over AP as well as the AP/

CNO, PANI/AP and PANI/AP/CNO composites; **c** XRD patterns of AP and PANI/AP/CNO before and after three cycles of the visible-light-driven degradation of RhB.

thereby enabling the faster separation and transfer of photogenerated electrons on the AP surface. In the latter case, due to their irregular growth, the AgNPs not only can not promote the transfer of electrons but actually hinder the degradation reaction.

To further study the relationship between the photocatalytic activity of PANI/AP/CNO and its structure, we separately performed the PL, transient photocurrent response and EIS Nyquist tests [29, 38, 59] (Fig. 5). The three test results consistently show that PANI/AP/CNO exhibits a better

separation efficiency of photogenerated charge carriers than the other three materials. Combined with the aforementioned photocatalytic activity results (Fig. 2a), these results clearly indicate that this novel AP–PANI–CNO structure improves the photocatalytic activity by enhancing the separation efficiency of the photogenerated charge carriers of AP.

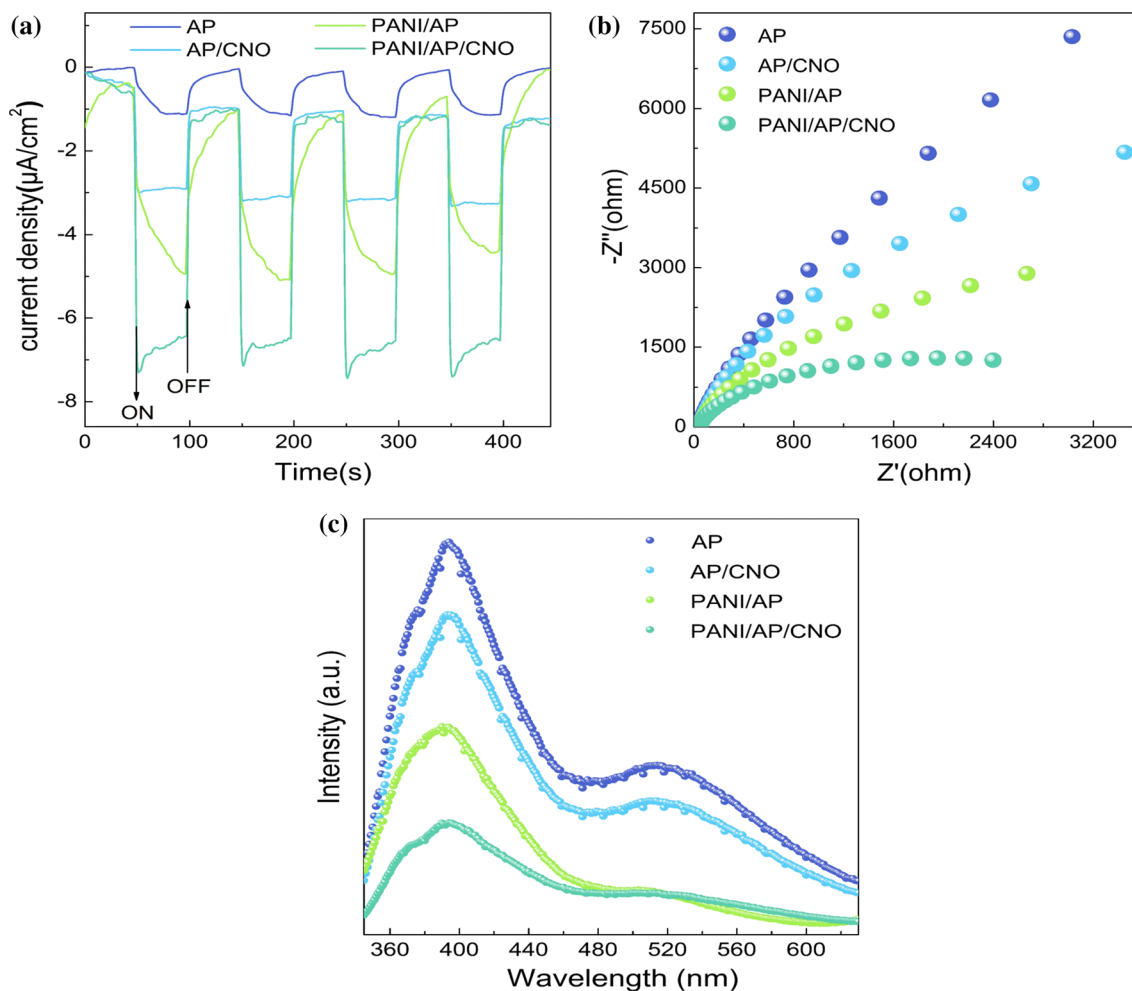


Figure 5 a Transient photocurrent response spectra; b EIS Nyquist plot; c photoluminescence spectra of AP as well as the AP/CNO, PANI/AP and PANI/AP/CNO composites.

Double Z-scheme heterojunction photocatalytic mechanism of PANI/AP/CNO

To further investigate how the PANI/AP/CNO system with a novel structure efficiently separates and transfers photogenerated electron–hole pairs of AP, we analysed the band structures of the three semiconductors in the PANI/AP/CNO heterojunction catalyst. As expected, the visible-light absorption performances of the three composites are improved compared with those of the three individual semiconductors (Fig. 6a). Among them, PANI/AP/CNO exhibits the best visible-light-harvesting performance; namely, it can more fully utilize solar radiation. Notably, the PANI also exhibits good visible-light-harvesting efficiency. However, employing the Kubelka–Munk equation: $\alpha h\nu = A (h\nu - E_g)^{n/2}$ [24], we calculated a forbidden band energy (E_g) of PANI

to be only 1.81 eV using plots of $(\alpha h\nu)^{1/2}$ versus energy ($h\nu$) [44] (Fig. 6b); that is, its photogenerated electron–hole pairs easily recombine. Similarly, we calculated the E_g values of AP and CNO to be 2.35 eV and 3.04 eV using plots of $(\alpha h\nu)^{1/2}$ versus energy ($h\nu$) [57] and $(\alpha h\nu)^2$ versus energy ($h\nu$) [31], respectively (Fig. 6c, d). In addition, for the purpose of determining the exact VB and CB positions of PANI, AP and CNO, we calculated the flat band potential (U_{fb}) values, which are used to approximate the CB of n-type semiconductors ($CB \approx U_{fb} - 0.2$ V) [58, 60], with values of -0.57 V, 0.25 V and -1.04 V versus SCE found, respectively, according to the intercept of the Mott–Schottky plot with the horizontal axis [61] (Fig. 6e–g). Additionally, the positive slope of the plots for PANI, AP and CNO showed their n-type nature, and thus, the CB potentials of PANI, Ag_3PO_4 and CNO were confirmed to be -0.53 V, 0.29 V and

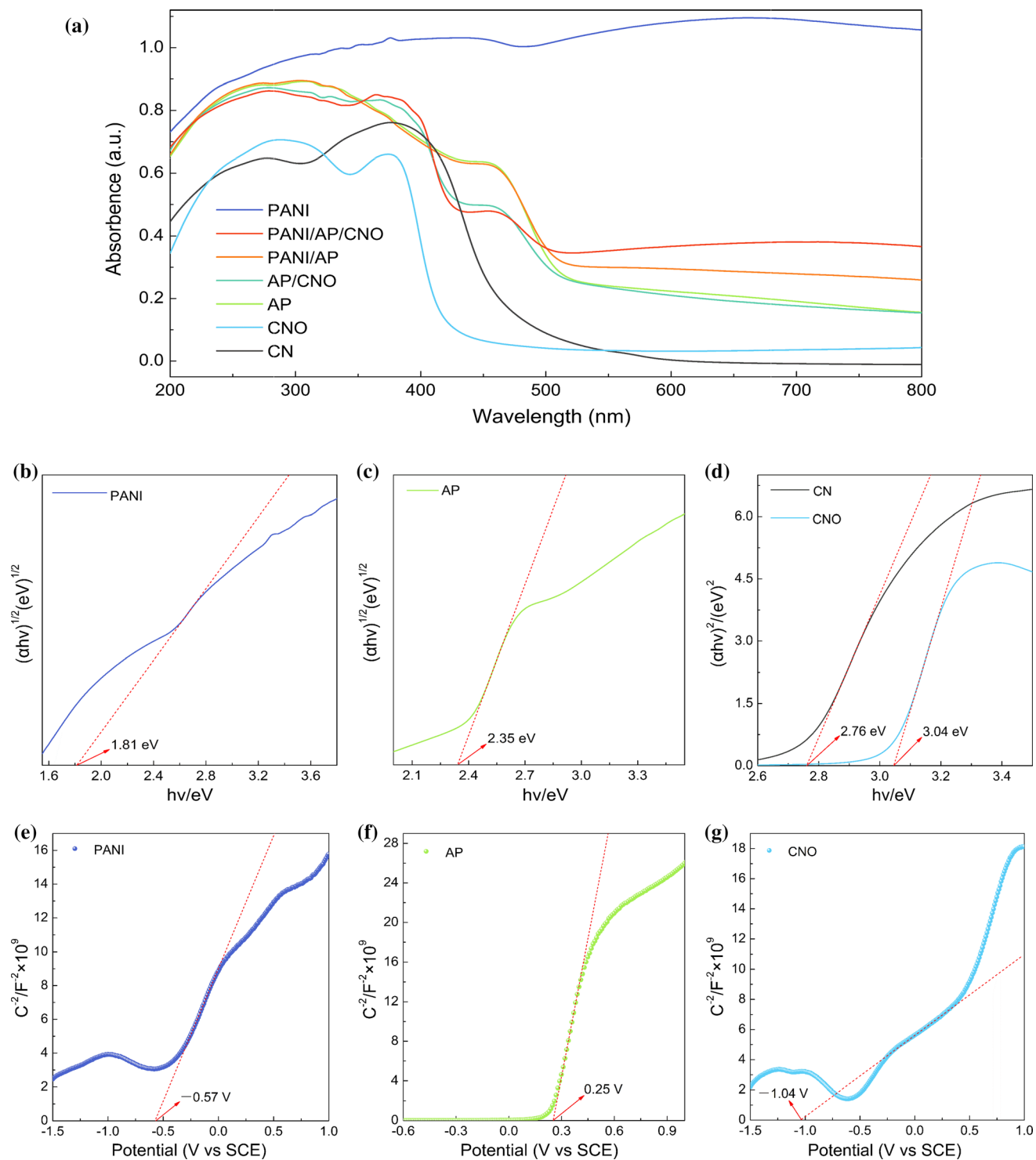


Figure 6 a UV-Vis DRS of PANI, CN, CNO and AP as well as the AP/CNO, PANI/AP and PANI/AP/CNO composites; Kubelka-Munk curves of **b** PANI, **c** AP and **d** CN and CNO; Mott-Schottky plots of **e** PANI, **f** AP and **g** CNO.

– 1.00 V versus normal hydrogen electrode (NHE, NHE = SCE + 0.24 V), and the values of VB were 1.28 V, 2.64 V and 2.04 V versus NHE, respectively.

We also carried out a series of free radical trapping experiments to explore the main active species produced by PANI/AP/CNO under visible-light exposure. As shown in Fig. 7a, after the addition of 1 mM

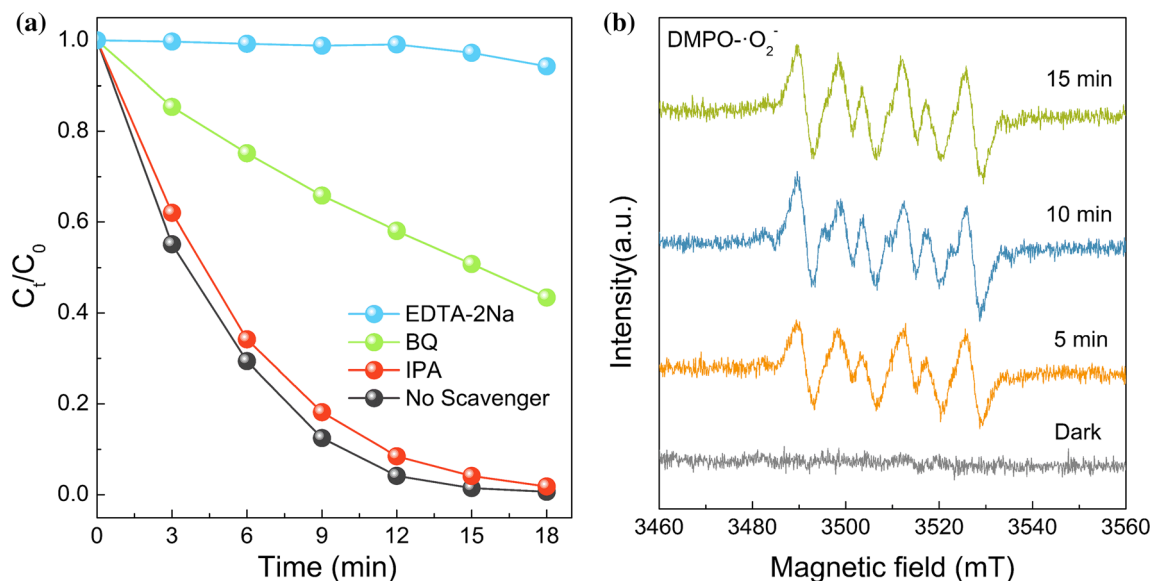


Figure 7 a Time profiles of the visible-light-driven degradation of RhB with the addition of scavengers over PANI/AP/CNO; b ESR spectra of ·O₂⁻ trapped by DMPO in the PANI/AP/CNO methanol

dispersion under both the dark and visible-light irradiation (> 420 nm, 300 W xenon lamp) conditions.

ethylenediaminetetraacetic acid disodium salt (EDTA-2Na functions as a trapping agent for h⁺ [62]) and 1 mM 1,4-benzoquinone (BQ functions as a trapping agent for ·O₂⁻ [63]), the rate of the degradation reaction decreased substantially, indicating that both h⁺ and ·O₂⁻ are main active substances produced by PANI/AP/CNO. Additionally, the generation of ·O₂⁻ is further confirmed by the EPR results. As shown in Fig. 7b, some characteristic peaks of DMPO-·O₂⁻ were observed in methanol dispersions of PANI/AP/CNO composites under visible-light irradiation. However, after the addition of 10 mM isopropanol (IPA functions as a trapping agent for ·OH [64]), the rate of the degradation reaction did not substantially decrease; thus, ·OH was not the main active substance produced by PANI/AP/CNO.

On the basis of these results, in combination with the aforementioned analyses of the band structures of the three semiconductors and the results of the free radical trapping tests, we propose a double Z-scheme heterojunction photocatalytic mechanism suitable for the PANI/AP/CNO system (Fig. 8). This mechanism is a good illustration of the process of the high-efficiency separation and transfer of photogenerated electron-hole pairs in a PANI/AP/CNO system with a novel structure. To further verify the rationality of the double Z-scheme heterojunction photocatalytic mechanism, we first assume that the

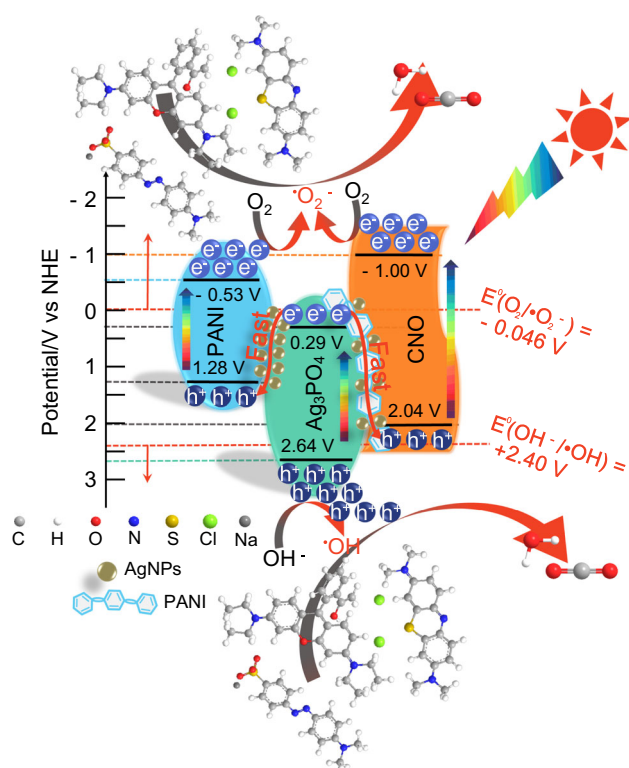


Figure 8 Double Z-scheme heterojunction photocatalytic mechanism of the PANI/AP/CNO composite under visible-light exposure.

system conforms to the conventional heterojunction photocatalytic mechanism (Fig. 9a). According to this mechanism, the photoproduced electrons and holes

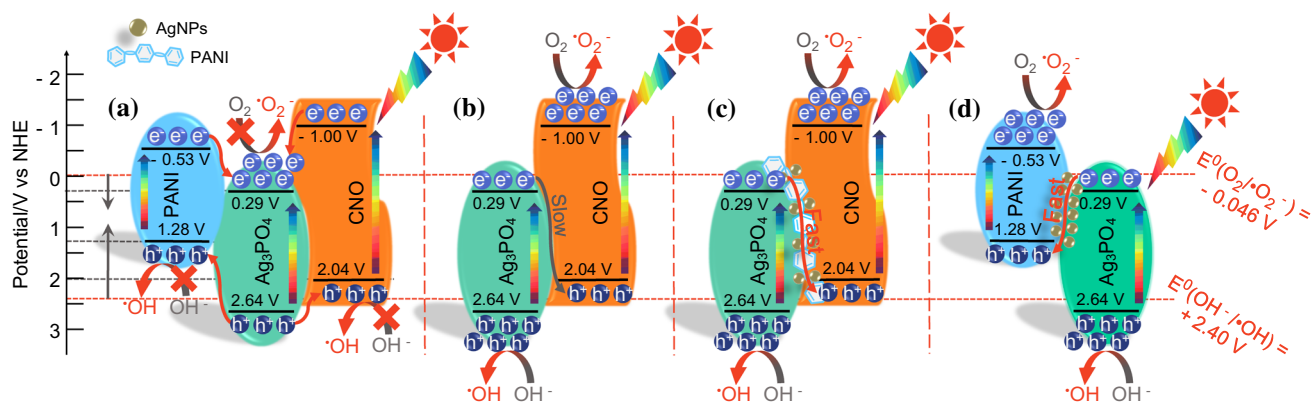
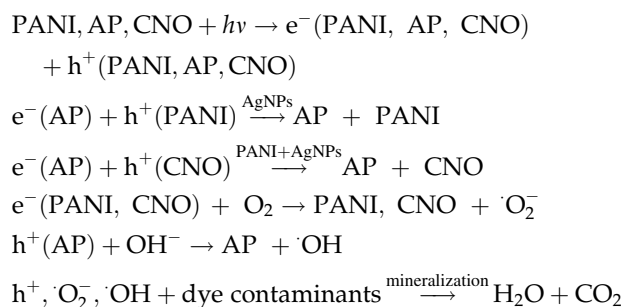


Figure 9 Diagrams of **a** the conventional heterojunction photocatalytic mechanism, **b** the direct Z-scheme heterojunction photocatalytic mechanism without PANI, **c** the all-solid Z-scheme heterojunction photocatalytic mechanism in which

gather on the CB of AP and the VB of PANI and CNO, respectively. Nevertheless, the photoproduced electrons on the CB of AP (+ 0.29 V vs. NHE) cannot reduce the free oxygen adsorbed onto the surface of PANI/AP/CNO to $\cdot\text{O}_2^-$ ($E^0(\text{O}_2/\text{O}_2^-) = -0.046$ V vs. NHE [28, 40]), which is conflicting with the results of the aforementioned scavenging experiments. Quite to the contrary, for the double Z-scheme heterojunction photocatalytic mechanism [65] (Fig. 8), the photoproduced holes on the VB of PANI and CNO recombine with the photoproduced electrons on the CB of AP, leading to holes gathering on the VB of AP (+ 2.64 V vs. NHE). These holes can not only oxidize hydroxyl ions adsorbed onto the surface of PANI/AP/CNO to $\cdot\text{OH}$ ($E^0(\text{OH}^-/\cdot\text{OH}) = +2.40$ V vs. NHE [19, 66]) but, more importantly, can immediately degrade dye contaminants, such as RhB, MO and MB, and eventually mineralize them into H_2O and CO_2 . Simultaneously, the electrons gathering on the CB of PANI (- 0.53 V vs. NHE) and CNO (- 1.00 V vs. NHE), respectively, can easily reduce oxygen to $\cdot\text{O}_2^-$, which is consistent with the results of the aforementioned capture experiments. Similarly, the generated $\cdot\text{O}_2^-$ and $\cdot\text{OH}$ can also directly participate in the degradation of dye contaminants and eventually mineralize them into H_2O and CO_2 . Notably, as shown in Fig. 2a, the degradation efficiency of PANI/AP/CNO is substantially higher than that of AP/CNO, which is likely the reason why the PANI organic film and the AgNPs generated in situ on its surface act as electron mediators between AP and CNO (Fig. 9c), effectively accelerating the electron transfer of the direct AP/CNO

PANI and its surface in situ grown AgNPs act as electron mediators and **d** the all-solid Z-scheme photocatalytic mechanism in which PANI surface and its surface in situ grown AgNPs act as electron mediators.

Z-scheme heterojunction (Fig. 9b), as indicated by the TEM image (Fig. 1d) and PL emission spectra (Fig. 5c). Additionally, PANI also functions as a photocatalyst in this system, and AgNPs generated in situ on its surface act as electron mediators [67] to accelerate the transfer of photogenerated electrons between PANI and AP (Fig. 9d). In short, the double Z-scheme heterojunction photocatalytic mechanism dramatically enhanced the lifetime of the photogenerated electron-hole pairs of AP, which was conducive to its activity and stability. The overall double Z-scheme heterojunction photocatalytic mechanism can be depicted as follows:



Conclusions

In conclusion, an AP material heterojunction with PANI and CNO exhibited outstanding activity in the visible-light-driven degradation of organic dye contaminants. With this catalyst, the degradation efficiency for RhB reached 98.54% in only 18 min, and the TOC removal efficiency for the mixture of RhB,

MB and MO also reached 85.24% in 180 min. Some characterizations, such as TEM and PL spectroscopy, were used to demonstrate this novel AP–PANI–CNO structure; in particular, both PANI and its surface in situ grown AgNPs in this system act as electron mediators, which suppress the formation of irregular metallic silver on the surface of AP and the recombination of photogenerated current carriers, ultimately improving the activity of the catalyst. Then, by researching the band structures of the three semiconductors and analysing the results of free radical trapping experiments, we proposed and confirmed a double Z-scheme heterojunction photocatalytic mechanism suitable for this system. This work provides a novel approach to degrading organic dyestuff with high activity and stability, particularly with clean and sustainable light energy.

Acknowledgements

This work was not supported by a commercial, nonprofit or public entity.

Compliance with ethical standards

Conflict of interest There are no conflicts of interest to declare.

Electronic supplementary material: The online version of this article (<https://doi.org/10.1007/s10853-019-04252-7>) contains supplementary material, which is available to authorized users.

References

- [1] Tong H, Ouyang S, Bi Y, Umezawa N, Oshikiri M, Ye J (2012) Nano-photocatalytic materials: possibilities and challenges. *Adv Mater* 24:229–251
- [2] Chen C, Ma W, Zhao J (2010) Semiconductor-mediated photodegradation of pollutants under visible-light irradiation. *Chem Soc Rev* 39:4206–4219
- [3] Wang H, Zhang L, Chen Z, Hu J, Li S, Wang Z, Liu J, Wang X (2014) Semiconductor heterojunction photocatalysts: design, construction, and photocatalytic performances. *Chem Soc Rev* 43:5234–5244
- [4] Low J, Yu J, Jaroniec M, Wageh S, Al-Ghamdi AA (2017) Heterojunction photocatalysts. *Adv Mater* 29:1601694
- [5] Marschall R (2014) Semiconductor composites: strategies for enhancing charge carrier separation to improve photocatalytic activity. *Adv Funct Mater* 24:2421–2440
- [6] Yi Z, Ye J, Kikugawa N, Kako T, Ouyang S, Stuart-Williams H, Yang H, Cao J, Luo W, Li Z, Liu Y, Withers RL (2010) An orthophosphate semiconductor with photooxidation properties under visible-light irradiation. *Nat Mater* 9:559–564
- [7] Ghazalian E, Ghasemi N, Amani-Ghadim AR (2017) Effect of gadollunium doping on visible light photocatalytic performance of Ag_3PO_4 : evaluation of activity in degradation of an anthraquinone dye and mechanism study. *J Mol Catal A Chem* 426:257–270
- [8] Martin DJ, Liu G, Moniz SJA, Bi Y, Beale AM, Ye J, Tang J (2015) Efficient visible driven photocatalyst, silver phosphate: performance, understanding and perspective. *Chem Soc Rev* 44:7808–7828
- [9] Teng F, Liu Z, Zhang A, Li M (2015) Photocatalytic performances of Ag_3PO_4 polypods for degradation of dye pollutant under natural indoor weak light irradiation. *Environ Sci Technol* 49:9489–9494
- [10] Liu Z, Liu Y, Xu P, Ma Z, Wang J, Yuan H (2017) Rational design of wide spectral-responsive heterostructures of Au nanorod coupled Ag_3PO_4 with enhanced photocatalytic performance. *ACS Appl Mater Interfaces* 9:20620–20629
- [11] Guo S, Jiang Y, Wu F, Yu P, Liu H, Li Y, Mao L (2018) Graphdiyne-promoted highly efficient photocatalytic activity of graphdiyne/silver phosphate pickering emulsion under visible-light irradiation. *ACS Appl Mater Interfaces* 11:2684–2691
- [12] Zhang H, Huang H, Ming H, Li H, Zhang L, Liu Y, Kang Z (2012) Carbon quantum dots/ Ag_3PO_4 complex photocatalysts with enhanced photocatalytic activity and stability under visible light. *J Mater Chem* 22:10501–10506
- [13] Yang X, Cui H, Li Y, Qin J, Zhang R, Tang H (2013) Fabrication of Ag_3PO_4 -graphene composites with highly efficient and stable visible light photocatalytic performance. *ACS Catal* 3:363–369
- [14] Abroshan E, Farhadi S, Zabardasti A (2018) Novel magnetically separable $\text{Ag}_3\text{PO}_4/\text{MnFe}_2\text{O}_4$ nanocomposite and its high photocatalytic degradation performance for organic dyes under solar-light irradiation. *Sol Energy Mater Sol Cells* 178:154–163
- [15] Yang Z, Huang G, Huang W, Wei J, Yan X, Liu Y, Jiao C, Wan Z, Pan A (2014) Novel $\text{Ag}_3\text{PO}_4/\text{CeO}_2$ composite with high efficiency and stability for photocatalytic applications. *J Mater Chem A* 2:1750–1756
- [16] Yang J, Hu R, Meng W, Du Y (2016) A novel p-LaFeO₃/n- Ag_3PO_4 heterojunction photocatalyst for phenol degradation

- under visible light irradiation. *Chem Commun* 52:2620–2623
- [17] Liu X, Xu J, Ni Z, Wang R, You J, Guo R (2019) Adsorption and visible-light-driven photocatalytic properties of $\text{Ag}_3\text{PO}_4/\text{WO}_3$ composites: a discussion of the mechanism. *Chem Eng J* 356:22–33
- [18] Wan J, Du X, Liu E, Hu Y, Fan J, Hu X (2017) Z-scheme visible-light-driven Ag_3PO_4 nanoparticle@ MoS_2 quantum dot/few-layered MoS_2 nanosheet heterostructures with high efficiency and stability for photocatalytic selective oxidation. *J Catal* 345:281–294
- [19] Shi W, Guo F, Yuan S (2017) In situ synthesis of Z-scheme $\text{Ag}_3\text{PO}_4/\text{CuBi}_2\text{O}_4$ photocatalysts and enhanced photocatalytic performance for the degradation of tetracycline under visible light irradiation. *Appl Catal B Environ* 209:720–728
- [20] Zhou P, Yu J, Jaroniec M (2014) All-solid-state Z-scheme photocatalytic systems. *Adv Mater* 26:4920–4935
- [21] Low J, Dai B, Tong T, Jiang C, Yu J (2018) In situ irradiated X-ray photoelectron spectroscopy investigation on a direct Z-scheme TiO_2/CdS composite film photocatalyst. *Adv Mater* 31:e1802981
- [22] Wang X, Maeda K, Thomas A, Takanabe K, Xin G, Carlsson JM, Domen K, Antonietti M (2009) A metal-free polymeric photocatalyst for hydrogen production from water under visible light. *Nat Mater* 8:76–80
- [23] Liu J, Liu Y, Liu N, Han Y, Zhang X, Huang H, Lifshitz Y, Lee S, Zhong J, Kang Z (2015) Metal-free efficient photocatalyst for stable visible water splitting via a two-electron pathway. *Science* 347:970–974
- [24] Hong Y, Jiang Y, Li C, Fan W, Yan X, Yan M, Shi W (2016) In-situ synthesis of direct solid-state Z-scheme $\text{V}_2\text{O}_5/\text{g-C}_3\text{N}_4$ heterojunctions with enhanced visible light efficiency in photocatalytic degradation of pollutants. *Appl Catal B Environ* 180:663–673
- [25] Liu G, Niu P, Sun C, Smith SC, Chen Z, Lu G, Cheng H (2010) Unique electronic structure induced high photoreactivity of sulfur-doped graphitic C_3N_4 . *J Am Chem Soc* 132:11642–11648
- [26] Chu S, Wang Y, Guo Y, Feng J, Wang C, Luo W, Fan X, Zou Z (2013) Band structure engineering of carbon nitride: in search of a polymer photocatalyst with high photooxidation property. *ACS Catal* 3:912–919
- [27] Chen X, Huang X, Yi Z (2014) Enhanced ethylene photodegradation performance of $\text{g-C}_3\text{N}_4\text{-Ag}_3\text{PO}_4$ composites with direct Z-scheme configuration. *Chem Eur J* 20:17590–17596
- [28] He Y, Zhang L, Teng B, Fan M (2014) New application of Z-Scheme $\text{Ag}_3\text{PO}_4/\text{g-C}_3\text{N}_4$ composite in converting CO_2 to fuel. *Environ Sci Technol* 49:649–656
- [29] Sun M, Zeng Q, Zhao X, Shao Y, Ji P, Wang C, Yan T, Du B (2017) Fabrication of novel $\text{g-C}_3\text{N}_4$ nanocrystals decorated Ag_3PO_4 hybrids: enhanced charge separation and excellent visible-light driven photocatalytic activity. *J Hazard Mater* 339:9–21
- [30] Yu W, Chen J, Shang T, Chen L, Gu L, Peng T (2017) Direct Z-scheme $\text{g-C}_3\text{N}_4/\text{WO}_3$ photocatalyst with atomically defined junction for H_2 production. *Appl Catal B Environ* 219:693–704
- [31] Di T, Zhu B, Cheng B, Yu J, Xu J (2017) A direct Z-scheme $\text{g-C}_3\text{N}_4/\text{SnS}_2$ photocatalyst with superior visible-light CO_2 reduction performance. *J Catal* 352:532–541
- [32] He R, Zhou J, Fu H, Zhang S, Jiang C (2018) Room-temperature in situ fabrication of $\text{Bi}_2\text{O}_3/\text{g-C}_3\text{N}_4$ direct Z-scheme photocatalyst with enhanced photocatalytic activity. *Appl Surf Sci* 430:273–282
- [33] Iwase A, Ng YH, Ishiguro Y, Kudo A, Amal R (2011) Reduced graphene oxide as a solid-state electron mediator in Z-scheme photocatalytic water splitting under visible light. *J Am Chem Soc* 133:11054–11057
- [34] Wang Q, Hisatomi T, Jia Q, Tokudome H, Zhong M, Wang C, Pan Z, Takata T, Nakabayashi M, Shibata N, Li Y, Sharp ID, Kudo A, Yamada T, Domen K (2016) Scalable water splitting on particulate photocatalyst sheets with a solar-to-hydrogen energy conversion efficiency exceeding 1%. *Nat Mater* 15:611–615
- [35] Tada H, Mitsui T, Kiyonaga T, Akita T, Tanaka K (2006) All-solid-state Z-scheme in CdS-Au-TiO_2 three-component nanojunction system. *Nat Mater* 5:782–786
- [36] Deng J, Liu L, Niu T, Sun X (2017) Synthesis and characterization of highly efficient and stable $\text{Pr}_6\text{O}_{11}/\text{Ag}_3\text{PO}_4/\text{Pt}$ ternary hybrid structure. *Appl Surf Sci* 403:531–539
- [37] Zhou S, Wang Z, Zhao Z, Shi S, Yan Z, Zou (2018) A facet-dependent Schottky-junction electron shuttle in a $\text{BiVO}_4\{010\}\text{-Au-Cu}_2\text{O}$ Z-scheme photocatalyst for efficient charge separation. *Adv Funct Mater* 28:1801214
- [38] Si H, Mao C, Zhou J, Rong X, Deng Q, Chen S, Zhao J, Sun X, Shen Y, Feng W, Gao P, Zhang J (2018) Z-scheme $\text{Ag}_3\text{PO}_4/\text{graphdiyne}/\text{g-C}_3\text{N}_4$ composites: enhanced photocatalytic O_2 generation benefiting from dual roles of graphdiyne. *Carbon* 132:598–605
- [39] Jo WK, Selvam NC (2017) Z-scheme $\text{CdS}/\text{g-C}_3\text{N}_4$ composites with RGO as an electron mediator for efficient photocatalytic H_2 production and pollutant degradation. *Chem Eng J* 317:913–924
- [40] Zhang J, Guo Y, Xiong Y, Zhou D, Dong S (2017) An environmentally friendly Z-scheme $\text{WO}_3/\text{CDots}/\text{CdS}$ heterostructure with remarkable photocatalytic activity and anti-photocorrosion performance. *J Catal* 356:1–13

- [41] Kim M, Lee C, Jang J (2014) Fabrication of highly flexible, scalable, and high-performance supercapacitors using polyaniline/reduced graphene oxide film with enhanced electrical conductivity and crystallinity. *Adv Funct Mater* 24:2489–2499
- [42] Wu Q, Xu Y, Yao Z, Liu A, Shi G (2010) Supercapacitors based on flexible graphene/polyaniline nanofiber composite films. *ACS Nano* 4:1963–1970
- [43] Jiang W, Luo W, Zong R, Yao W, Li Z, Zhu Y (2016) Polyaniline/carbon nitride nanosheets composite hydrogel: a separation-free and high-efficient photocatalyst with 3D hierarchical structure. *Small* 12:4370–4378
- [44] Liu L, Ding L, Liu Y, An W, Lin S, Liang Y, Cui W (2017) A stable Ag_3PO_4 @PANI core@shell hybrid: enrichment photocatalytic degradation with π - π conjugation. *Appl Catal B Environ* 201:92–104
- [45] Bu Y, Chen Z (2014) Role of polyaniline on the photocatalytic degradation and stability performance of the polyaniline/silver/silver phosphate composite under visible light. *ACS Appl Mater Interfaces* 6:17589–17598
- [46] Chen F, Wu Y, Ning J, Ren J, Zhang Z, Zheng C, Zhong Y, Hu Y (2017) Facile preparation of ternary $\text{Ag}_2\text{CO}_3/\text{Ag}/\text{PANI}$ composite nanorods with enhanced photoactivity and stability. *J Mater Sci* 52:4521–4531. <https://doi.org/10.1007/s10853-016-0697-7>
- [47] She X, Wu J, Zhong J, Xu H, Yang Y, Vajtai R, Lou J, Liu Y, Du D, Li H, Ajayan PM (2016) Oxygenated monolayer carbon nitride for excellent photocatalytic hydrogen evolution and external quantum efficiency. *Nano Energy* 27:138–146
- [48] Yang X, Chen Z, Xu J, Tang H, Chen K, Jiang Y (2015) Tuning the morphology of $\text{g-C}_3\text{N}_4$ for Improvement of Z-scheme photocatalytic water oxidation. *ACS Appl Mater Interfaces* 7:15285–15293
- [49] Chang G, Luo Y, Lu W, Qin X, Asiri AM, Al-Youbi AO, Sun X (2012) Ag nanoparticles decorated polyaniline nanofibers: synthesis, characterization, and applications toward catalytic reduction of 4-nitrophenol and electrochemical detection of H_2O_2 and glucose. *Catal Sci Technol* 2:800–806
- [50] Liu W, Shen J, Yang X, Liu Q, Tang H (2018) Dual Z-scheme $\text{g-C}_3\text{N}_4/\text{Ag}_3\text{PO}_4/\text{Ag}_2\text{MoO}_4$ ternary composite photocatalyst for solar oxygen evolution from water splitting. *Appl Surf Sci* 456:369–378
- [51] Jiang J, Ou-yang L, Zhu L, Zheng A, Zou J, Yi X, Tang H (2014) Dependence of electronic structure of $\text{g-C}_3\text{N}_4$ on the layer number of its nanosheets: a study by Raman spectroscopy coupled with first-principles calculations. *Carbon* 80:213–221
- [52] Nie N, Zhang L, Fu J, Cheng B, Yu J (2018) Self-assembled hierarchical direct Z-scheme $\text{g-C}_3\text{N}_4/\text{ZnO}$ microspheres with enhanced photocatalytic CO_2 reduction performance. *Appl Surf Sci* 441:12–22
- [53] Liu J, Li W, Duan L, Li X, Ji L, Geng Z, Huang K, Lu L, Zhou L, Liu Z, Chen W, Liu L, Feng S, Zhang Y (2015) A graphene-like oxygenated carbon nitride material for improved cycle-life lithium/sulfur batteries. *Nano Lett* 15:5137–5142
- [54] Niu P, Zhang L, Liu G, Cheng H (2012) Graphene-like carbon nitride nanosheets for Improved photocatalytic activities. *Adv Funct Mater* 22:4763–4770
- [55] Zhang G, Li G, Lan Z, Lin L, Savateev A, Heil T, Zafeiratos S, Wang X, Antonietti M (2017) Optimizing optical absorption, exciton dissociation, and charge transfer of a polymeric carbon nitride with ultrahigh solar hydrogen production activity. *Angew Chem Int Ed* 129:13630–13634
- [56] Kim YG, Jo WK (2019) Efficient decontamination of textile industry wastewater using a photochemically stable n-n type $\text{CdSe}/\text{Ag}_3\text{PO}_4$ heterostructured nanohybrid containing metallic Ag as a mediator. *J Hazard Mater* 361:64–72
- [57] Cao W, Gui Z, Chen L, Zhu X, Qi Z (2017) Facile synthesis of sulfate-doped Ag_3PO_4 with enhanced visible light photocatalytic activity. *Appl Catal B Environ* 200:681–689
- [58] Cai T, Liu Y, Wang L, Zhang S, Zeng Y, Yuan J, Ma J, Dong W, Liu C, Luo S (2017) Silver phosphate-based Z-scheme photocatalytic system with superior sunlight photocatalytic activities and anti-photocorrosion performance. *Appl Catal B Environ* 208:1–13
- [59] Dong Z, Wu Y, Thirugnanam N, Li G (2018) Double Z-scheme $\text{ZnO}/\text{ZnS}/\text{g-C}_3\text{N}_4$ ternary structure for efficient photocatalytic H_2 production. *Appl Surf Sci* 430:293–300
- [60] Wang Y, Zeng Y, Wan S, Cai W, Song F, Zhang S, Zhong Q (2018) In situ fabrication of 3D octahedral $\text{g-C}_3\text{N}_4/\text{BiFeWO}_x$ double-heterojunction for highly selective CO_2 photoreduction to CO under visible light. *ChemCatChem* 10:4578–4585
- [61] Xu B, He P, Liu H, Wang P, Zhou G, Wang X (2014) A 1D/2D helical $\text{CdS}/\text{ZnIn}_2\text{S}_4$ nano-heterostructure. *Angew Chem Int Ed* 53:2339–2343
- [62] Liu Q, Shen J, Yang X, Zhang T, Tang H (2018) 3D reduced graphene oxide aerogel-mediated Z-scheme photocatalytic system for highly efficient solar-driven water oxidation and removal of antibiotics. *Appl Catal B Environ* 232:562–573
- [63] Zhu B, Xia P, Li Y, Ho W, Yu J (2017) Fabrication and photocatalytic activity enhanced mechanism of direct Z-scheme $\text{g-C}_3\text{N}_4/\text{Ag}_2\text{WO}_4$ photocatalyst. *Appl Surf Sci* 391:175–183
- [64] Madhusudan P, Zhang J, Yu J, Cheng B, Xu D, Zhang J (2016) One-pot template-free synthesis of porous CdMoO_4

- microspheres and their enhanced photocatalytic activity. *Appl Surf Sci* 387:202–213
- [65] Xu Q, Zhang L, Yu J, Wageh S, Al-Ghamdi AA, Jaroniec M (2018) Direct Z-scheme photocatalysts: principles, synthesis, and applications. *Mater Today* 21:1042–1063
- [66] Ma D, Wu J, Gao M, Xin Y, Sun Y, Ma T (2017) Hydrothermal synthesis of an artificial Z-scheme visible light photocatalytic system using reduced graphene oxide as the electron mediator. *Chem Eng J* 313:1567–1576
- [67] Cui X, Tian L, Xian X, Tang H, Yang X (2018) Solar photocatalytic water oxidation over $\text{Ag}_3\text{PO}_4/\text{g-C}_3\text{N}_4$ composite materials mediated by metallic Ag and graphene. *Appl Surf Sci* 430:108–115

Publisher's Note Springer Nature remains neutral with regard to jurisdictional claims in published maps and institutional affiliations.